science.sciencemag.org/cgi/content/full/science.abb2762/DC1

Supplementary Materials for

Structural basis for the recognition of the SARS-CoV-2 by full-length human ACE2

Renhong Yan, Yuanyuan Zhang*, Yaning Li*, Lu Xia, Yingying Guo, Qiang Zhou†

*These authors contributed equally to this work.
†Corresponding author. Email: zhouqiang@westlake.edu.cn

Published 4 March 2020 on *Science* First Release
DOI: 10.1126/science.abb2762

This PDF file includes:

Other Supporting Online Material for this manuscript includes the following:
(available at science.sciencemag.org/cgi/content/full/science.abb2762/DC1)

Materials and Methods

Protein preparation

The cDNAs for full-length human B^0AT1 (accession number: NM_001003841) and ACE2 (accession number: NM_001371415) were subcloned into pCAG respectively. An N-terminal FLAG tag was fused to B^0AT1, and one Strep tag was fused after the N-terminal signal peptide of ACE2 using a standard two-step PCR.

HEK 293F cells (Invitrogen) were cultured in SMM 293T-II medium (Sino Biological Inc.) at 37 °C under 5% CO_2 in a Multitron-Pro shaker (Infors, 130 rpm). To co-express B^0AT1 and ACE2, the cells were transiently transfected with the plasmids and polyethylenimines (PEIs) (Polysciences) when the cell density reached approximately 2.0×10^6/ml. For transfection one liter of cell culture, about 0.75 mg plasmids for B^0AT1 and 0.75 mg plasmids for ACE2 were premixed with 3 mg PEIs in 50 ml of fresh medium for 15 mins before adding to cell culture. The transfected cells were cultured for 48-60 hours before harvesting.

For purification of the B^0AT1 and ACE2 complex, the cells were collected in a buffer containing 25 mM Tris, pH 8.0, 150 mM NaCl, and three protease inhibitors , aprotinin (1.3 μg/ml, AMRESCO), pepstatin (0.7 μg/ml, AMRESCO), and leupeptin (5 μg/ml, AMRESCO). The membrane fraction was solubilized at 4 °C for 2 hours with 1% (w/v) glyco diosgenin (GDN, Anatrace) and the cell debris was removed by centrifugation at 18,700 g for 45 mins. The supernatant was loaded to anti-FLAG M2 affinity resin (Sigma). After rinsing with a wash buffer containing 25 mM Tris, pH 8.0, 150 mM NaCl, and 0.02% GDN (w/v), the protein was eluted with wash buffer plus 0.2 mg/ml FLAG peptide. The eluent was further purified by Strep-Tactin Sepharose (IBA). After eluted with the wash buffer supplemented with 4 mM desthiobiotin (IBA), the eluent was then concentrated and subject to size-exclusion chromatography (Superose 6 Increase 10/300 GL, GE Healthcare) in the buffer containing 25 mM Tris, pH 8.0, 150 mM NaCl, and 0.02% GDN. The peak fractions were collected and concentrated for EM analysis.

Cryo-EM sample preparation and data acquisition

For cryo-sample preparation, the purified ACE2-B^0AT1 complex was concentrated to ~ 8 mg/ml. For the RBD-ACE2-B^0AT1 complex, the purified ACE2-B^0AT1 complex was mixed with the RBD (residues 319-541) of the S protein of the SARS-CoV-2, which has a C-terminal mouse Fc tag (Sino Biological Inc.), at a molar ratio of about 1:1.1 in the presence of 10 mM leucine. After 2 hour-incubation, aliquots (3.3 μl) of the mixture were placed on glow-discharged holey carbon grids (Quantifoil Au R1.2/1.3), which were blotted for 3.0 s or 3.5 s and flash-frozen in liquid ethane cooled by liquid nitrogen with Vitrobot (Mark IV, Thermo Fisher Scientific). The cryo grids were transferred to a Titan Krios operating at 300 kV equipped with Gatan K3 Summit detector and GIF Quantum energy filter. Movie stacks were automatically collected using AutoEMation (*39*), with a slit width of 20 eV on the energy filter and a defocus range from -1.2 μm to -2.2 μm in super-resolution mode at a nominal magnification of 81,000×. Each stack was exposed for 2.56 s with an exposure time of 0.08 s per frame, resulting in a total of 32 frames per stack. The total dose rate was approximately 50 $e^-/Å^2$ for each stack. The stacks were motion corrected with MotionCor2 (*40*) and binned 2-fold, resulting in a pixel size of 1.087 Å/pixel. Meanwhile, dose weighting was performed (*41*). The defocus values were estimated with Gctf (*42*).

Data processing

Particles were automatically picked using Relion 3.0.6 (43-46) from manually selected micrographs. After 2D classification with Relion, good particles were selected and subject to 3D classification with Relion with C2 symmetry against an initial model generated with Relion (the ACE2-B^0AT1 complex). The open and closed conformation particles were selected and subject to local defocus correction (*42*), 3D auto-refinement and post-processing. To improve the map quality of the closed conformation, the dataset was further focused refined with adapted mask applied on the extracellular region and the TM region, respectively. For TM region, the dataset was symmetry-expanded before refinement. For the dataset of the open conformation

of the ACE2-B^0AT1 complex, the dataset was further subject to 2 rounds of heterogeneous refinement and non-uniform refinement with cryoSPARC (*47*).
For the RBD-ACE2-B^0AT1 complex, the methods for particle picking and 2D classification are same to that for ACE2-B^0AT1 complex. The good particles selected from 2D classification are subject to three cycles of heterogeneous refinement with C1 symmetry using cryoSPARC. The good particles were selected and subject to homogeneous refinement with C2 symmetry, resulting in the 3D reconstruction for the whole structure. The map quality in the extracellular region or in the TM region was improved by focused refinement with Relion. To further improve the map quality for RBD and the binding interface between ACE2 and RBD, the particles were C2-symmetry expanded and re-centered at the location of the interface between ACE2 and RBD. The re-extracted dataset was 3D classified with Relion focused on the interface between ACE2 and RBD. Then the good particles were selected and subject to focused refinement with Relion, resulting in the 3D reconstruction of better quality on the binding interface and RBD.
The resolution was estimated with the gold-standard Fourier shell correlation 0.143 criterion (*48*) with high-resolution noise substitution (*49*). Refer to Supplemental Figures S1-S3,S5-S6 and Supplemental Table S1 for details of data collection and processing.

Model building and structure refinement

Model building of the ACE2-B^0AT1 complex was performed by molecular dynamics flexible fitting (MDFF) (*50*) of the published structure (PDB ID: 6ACJ) for the PD domain of ACE2 or *ab initio* with Phenix (*51*) and Coot (*52*) for the other parts based on the focused-refined cryo-EM maps with aromatic residues as landmarks, most of which were clearly visible in the cryo-EM map. Each residue was manually checked with the chemical properties taken into consideration during model building. Several segments, whose corresponding densities were invisible, were not modeled.
For the RBD-ACE2-B^0AT1 complex, the model building was accomplished based on the focused refined maps of the ternary complex. For the ACE2- B^0AT1 complex part

and RBD part, the model of the ACE2- B^0AT1 complex described above and the atomic model of SARS-RBD (PDB ID: 2AJF) was used as template, respectively. Structural refinement was performed in Phenix with secondary structure and geometry restraints to prevent overfitting. To monitor the potential overfitting, the model was refined against one of the two independent half maps from the gold-standard 3D refinement approach. Then, the refined model was tested against the other map. Statistics associated with data collection, 3D reconstruction and model building is summarized in Table S1.

Supplementary Figures and Legends

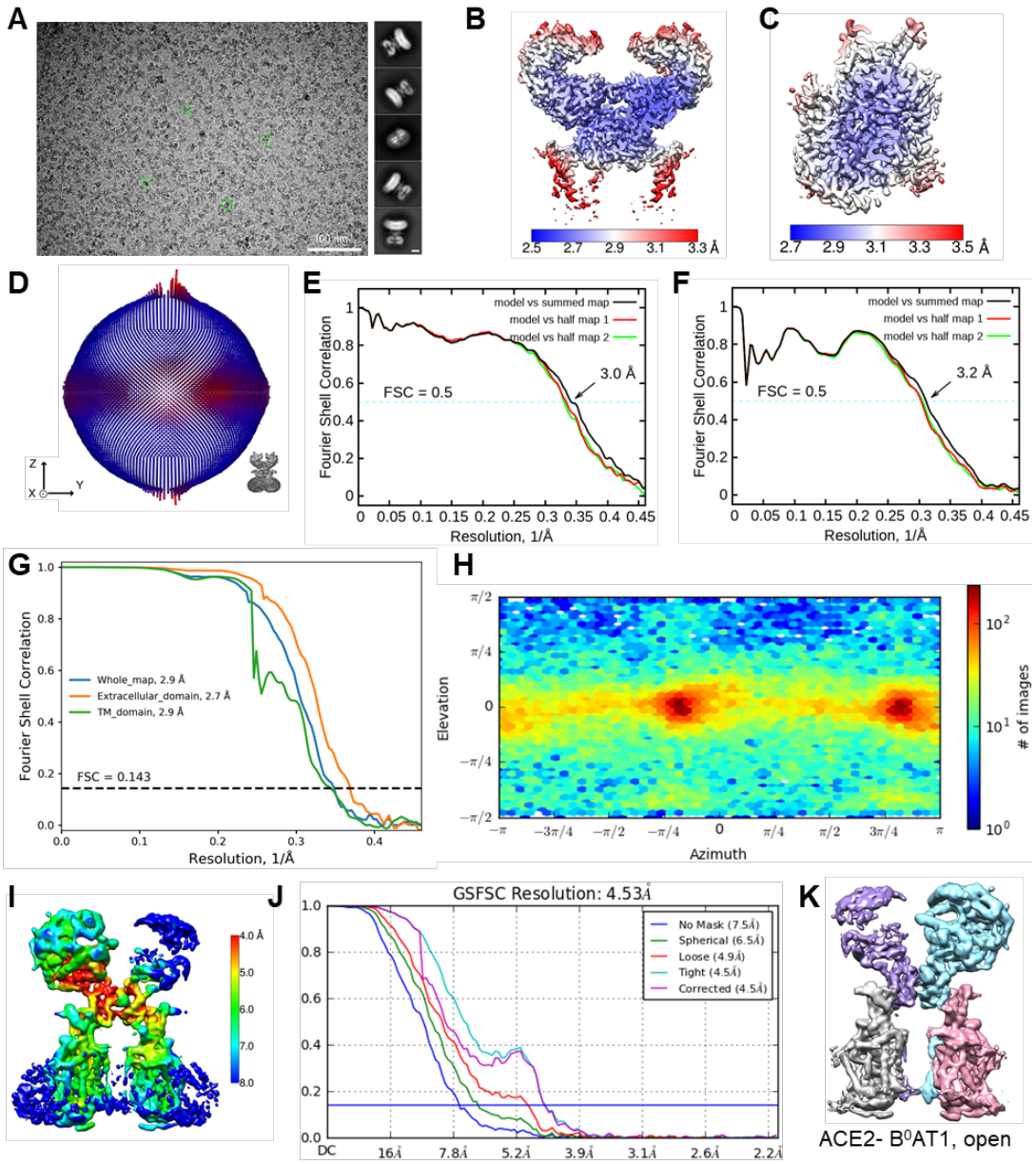

Fig. S1

Cryo-EM analysis of ACE2-B^{0}AT1 complex in closed and open conformation.

(A) Representative electron micrograph and 2D class averages of cryo-EM particle images. The scale bar in 2D class averages represents 10 nm. **(B)** and **(C)** Local resolution map for the 3D reconstruction of extracellular region and TM region of closed ACE2-B^{0}AT1 complex. **(D)** Euler angle distribution of closed ACE2-B^{0}AT1 complex in the final 3D reconstruction. **(E)** FSC curve of the refined model of closed ACE2-B^{0}AT1 versus the extracellular region that it is refined against (black);

of the model refined against the first half map versus the same map (red); and of the model refined against the first half map versus the second half map (green). The small difference between the red and green curves indicates that the refinement of the atomic coordinates did not suffer from overfitting. **(F)** FSC curve of the refined model of TM region of closed ACE2-B^0AT1 complex, which is the same as the (E). **(G)** Gold standard FSC curves of the overall structure (blue), extracellular region (orange) and TM region (green) of closed ACE2-B^0AT1 complex. **(H)** Euler angle distribution of open ACE2-B^0AT1 complex in the final 3D reconstruction in cryoSPARC. **(I)** Local resolution map for the 3D reconstruction of open ACE2-B^0AT1 complex. **(J)** Gold standard FSC curve of open ACE2-B^0AT1 complex is estimated by cryoSPARC. **(K)** Cryo-EM map of the ACE2-B^0AT1 complex in the open conformation. The map is coloured by subunits.

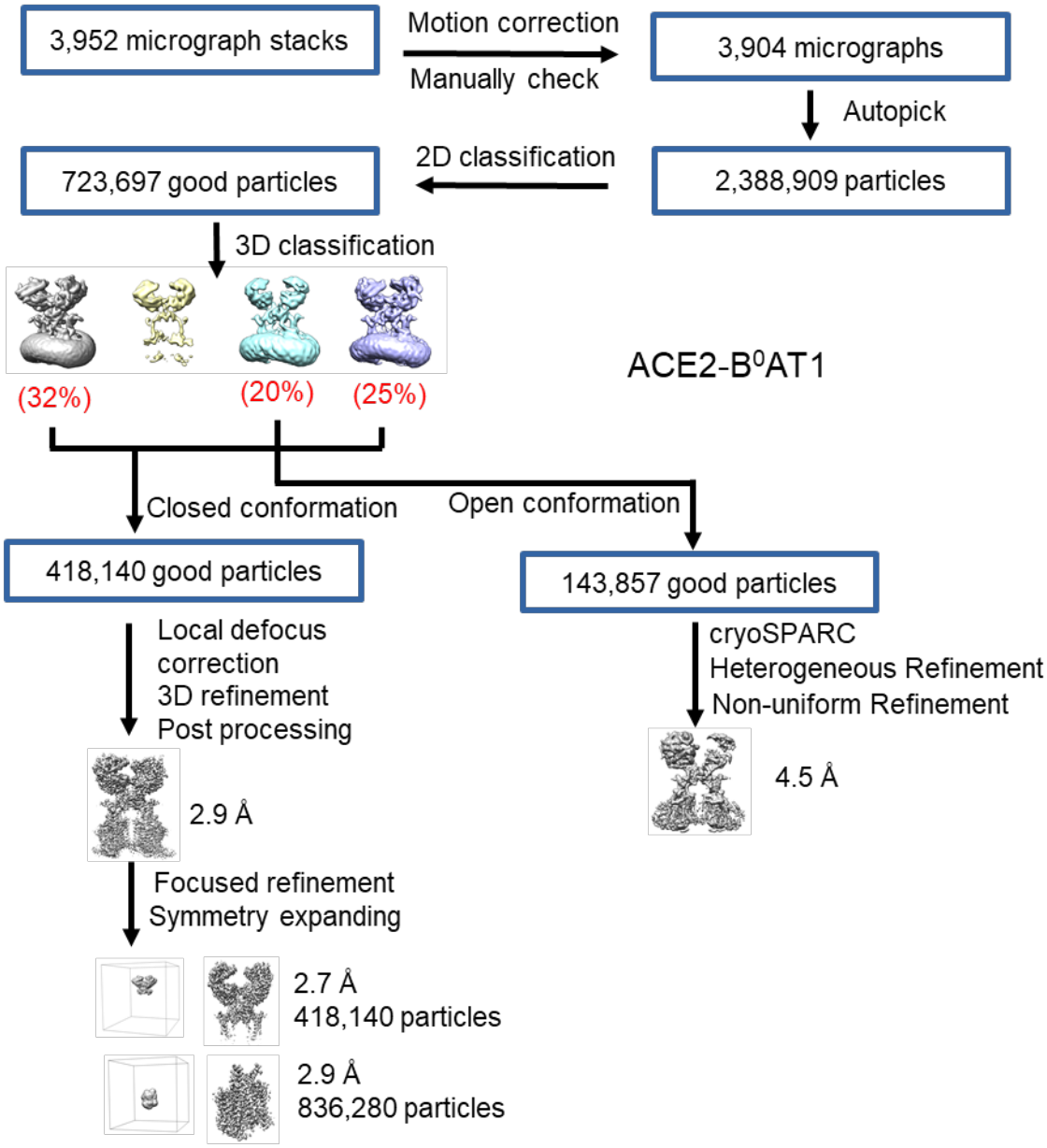

Fig. S2

Flowchart for cryo-EM data processing for ACE2-B^{0}AT1 complex.

Please see the "Data Processing" section in Methods for details.

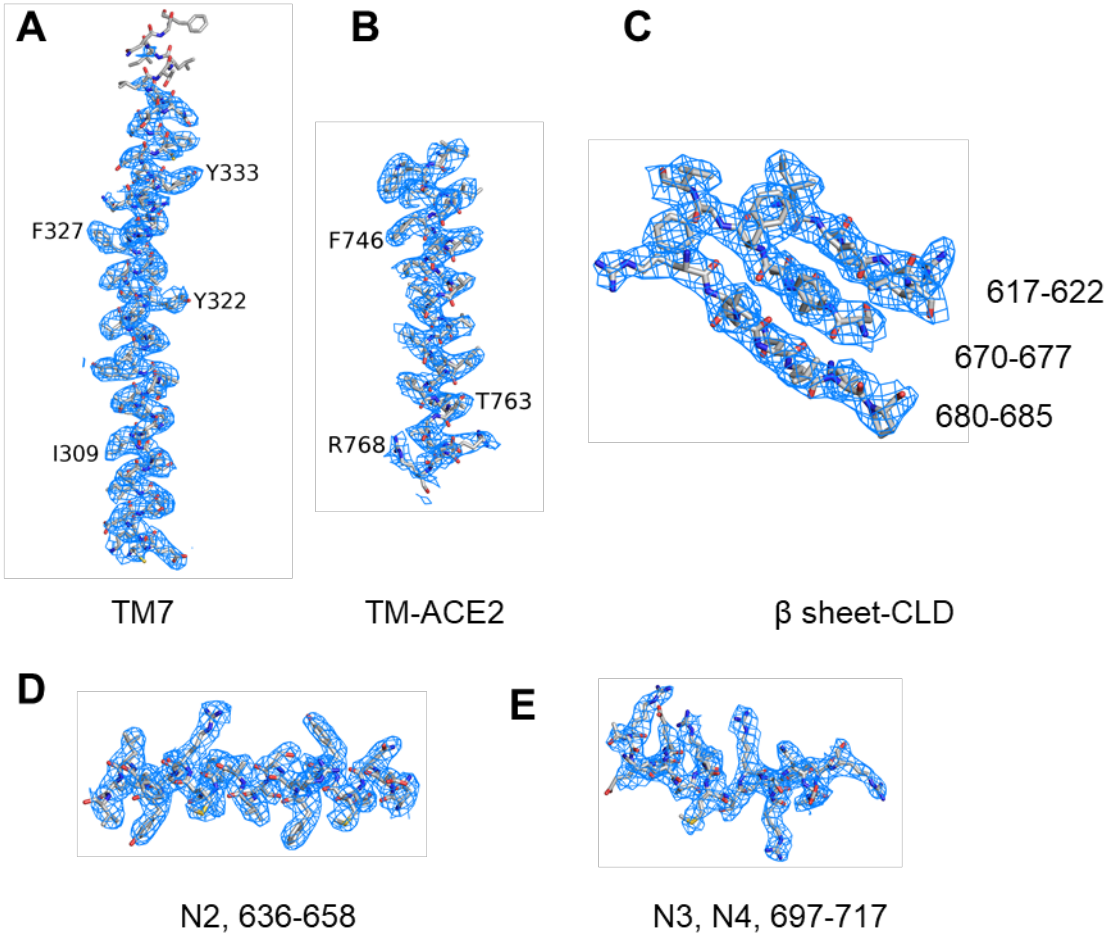

Fig. S3

Representative Cryo-EM densities.

Shown here are the cryo-EM maps of indicated segments of ACE2-B^0AT1 complex in the closed conformation. All densities are generated in PyMOL and contoured at 8 σ.

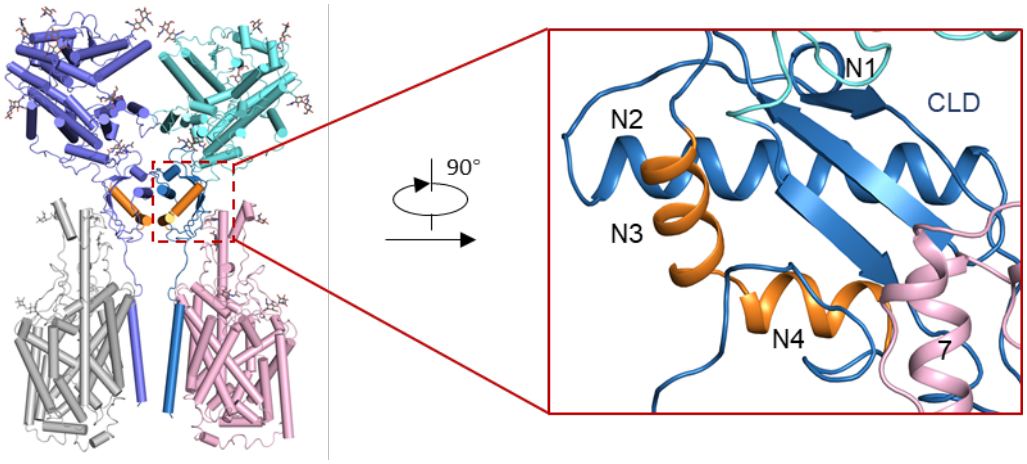

Fig. S4

Structure of the Neck domain in CLD.

The Neck domain exhibits a ferredoxin-like fold. The four α-helices in CLD are labelled N1-N4. The segment containing the predicted cleavage site is colored orange.

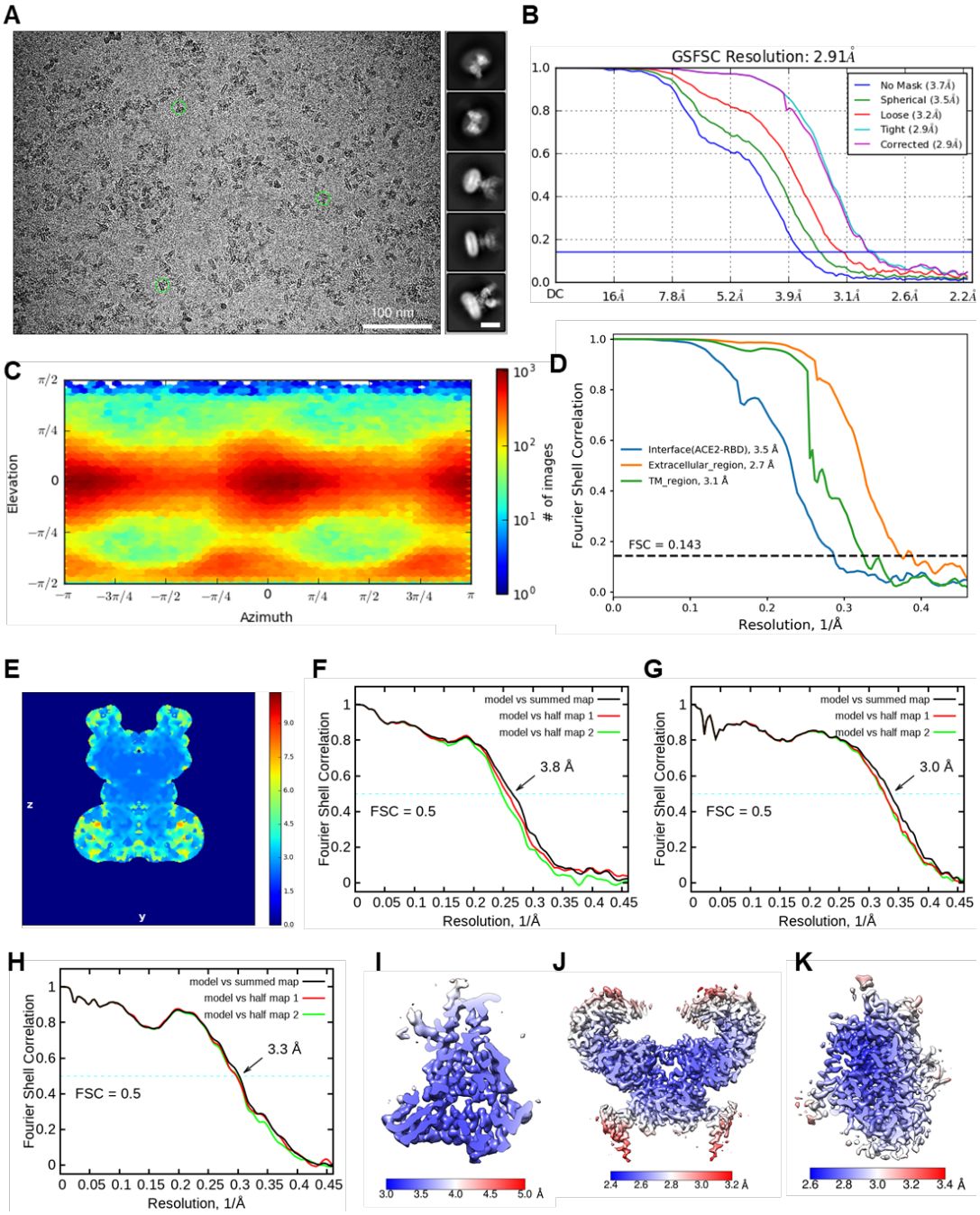

Fig. S5

Cryo-EM analysis of the RBD-ACE2-B^{0}AT1 ternary complex.

(A) Representative electron micrograph and 2D class averages of cryo-EM particle images. The scale bar in 2D class averages represents 10 nm. **(B)** Gold standard FSC curve of the cryoSPARC 3D reconstruction of the ternary complex. **(C)** Euler angle distribution of the ternary complex in the final cryoSPARC 3D reconstruction.

(D) Gold standard FSC curves of the interface between RBD and ACE2 (blue), TMcellular region (orange) and TM region (green) of the RBD-ACE2-B^0AT1 ternary complex. **(E)** Local resolution map for the 3D reconstruction of the whole structure of RBD-ACE2-B^0AT1 ternary complex. **(F)** FSC curve of the refined model of RBD-ACE2-B^0AT1 ternary complex versus the interface between RBD and ACE2 that it is refined against (black); of the model refined against the first half map versus the same map (red); and of the model refined against the first half map versus the second half map (green). The small difference between the red and green curves indicates that the refinement of the atomic coordinates did not suffer from overfitting. **(G)** and **(H)** are FSC curves of the refined model of extracellular region and TM region of RBD-ACE2-B^0AT1 ternary complex, which are the same as the (F), respectively. **(I)-(K)** are local resolution maps for the 3D reconstruction of the interface between RBD and ACE2, extracellular region and TM region of the RBD-ACE2-B^0AT1 ternary complex, respectively.

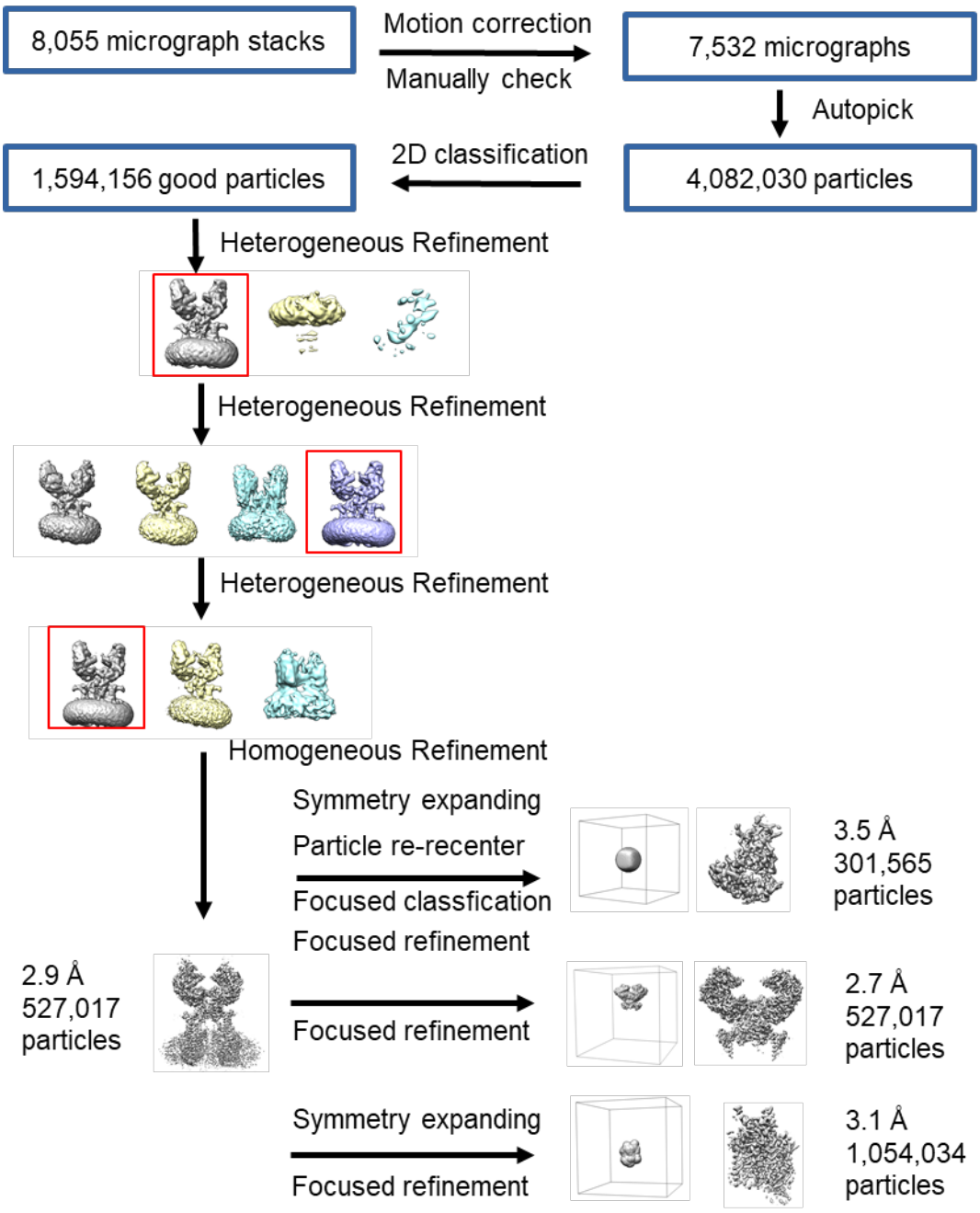

Fig. S6

Flowchart for cryo-EM data processing for RBD-ACE2-B^{0}AT1 ternary complex.

Please see the "Data Processing" section in Methods for details.

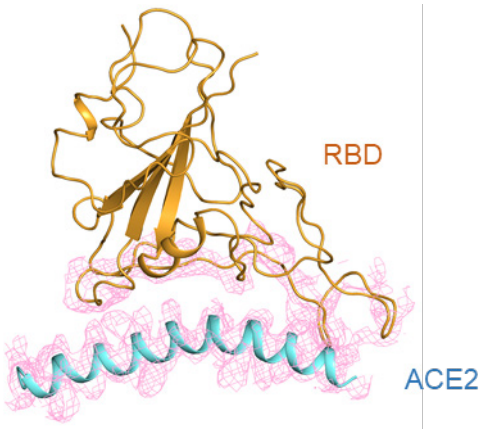

Fig. S7

Cryo-EM density of the interface between RBD and ACE2.

The density, shown as pink meshes, is contoured at 12 σ.

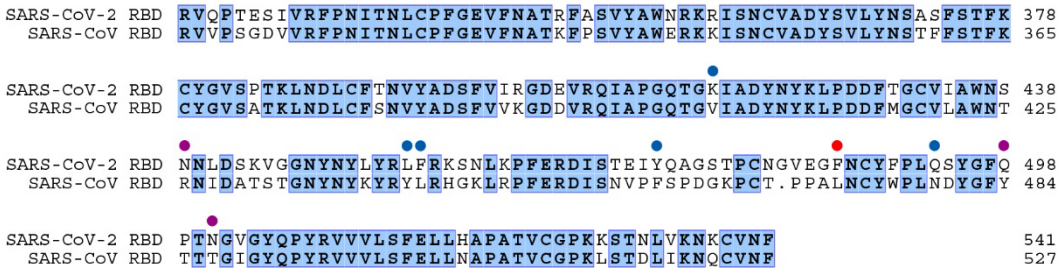

Fig. S8

Sequence alignment for the RBD of the S proteins from SARS-CoV-2 and SARS-CoV.

The two sequences were aligned using ClustalX. Invariant amino acids are shaded blue. The altered interface residues between nCoV-RBD and SARS-CoV RBD are indicated by solid circles and color-coded using the same scheme as for the boxes in Figure 4. The Uniprot IDs: SARS-CoV-2 S protein (P0DTC2) and SARS-CoV S protein (P59594).

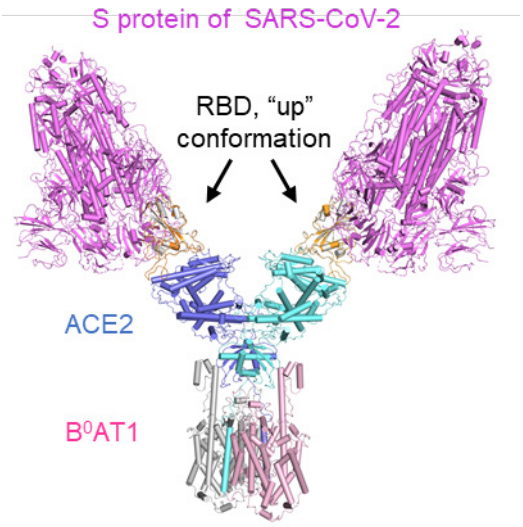

Fig. S9

Structural superimposition of the RBD-ACE2-B^0AT1 ternary complex with the S protein of SARS-CoV-2 (PDB code: 6VSB).

In the trimeric S protein,one RBD exhibits "up" conformation and the other two are "down". Clash between ACE2 and the S protein can be avoided only when the ternary complex is superimposed to the "up" RBD, as shown here.

Table S1 Cryo-EM data collection and refinement statistics.

Data collection			
EM equipment	Titan Krios (Thermo Fisher Scientific)		
Voltage (kV)	300		
Detector	Gatan K3 Summit		
Energy filter	Gatan GIF Quantum, 20 eV slit		
Pixel size (Å)	1.087		
Electron dose (e-/Å2)	50		
Defocus range (μm)	-1.2 ~ -2.2		
Number of collected micrographs	3,952		8,055
Number of selected micrographs	3,904		7,532
Sample	ACE2- B^0AT1 complex		RBD-ACE2-B^0AT1 complex
3D Reconstruction			
Conformation	closed	open	closed
Software	Relion	cryoSPARC	cryoSPARC/Relion/ Relion/Relion [b]
Number of used particles	418,140/418,140/ 836,280 [a]	143,857	527,017/301,565/ 527,017/1054,034 [b]
Resolution (Å)	2.9/2.7/2.9 [a]	4.5	2.9/3.5/2.7/3.1 [b]
Symmetry	C2/C2/C1 [a]	C1	C2/C1/C2/C1 [b]
Map sharpening B factor ($Å^2$)	-90/-90/-150 [a]	-140	-118/-150/-90/-150 [b]
PDB code	6M18	6M1D	6M17
EMDB code	EMD-30040/ EMD-30044/ EMD-30045 [a]	EMD-30041	EMD-30039/ EMD-30046/ EMD-30042/ EMD-30043 [b]
Refinement			
Software	Phenix		
Cell dimensions (Å)	313.056		
Model composition			
Protein residues	2,708	2,708	3,078
Side chains assigned	2,708	2,708	3,078
Sugar	38	N/A	44
Phospholipid	4	N/A	N/A
Zn	2	N/A	2
Water	30	N/A	8
RMSD			
Bonds length (Å)	0.01	0.005	0.008
Bonds Angle (°)	1.085	1.123	1.187
Ramachandran plot statistics (%)			
Preferred	91.11	90.55	91.01
Allowed	8.74	9.30	8.53
Outlier	0.15	0.15	0.46

[a]whole structure/ extracellular region/ TM region

[b]whole structure/ interface between RBD and ACE2/ extracellular region/ TM region

Movie S1

The structural morph between the closed and open conformation of the ACE2-B^0AT1 complex.

References and notes

1. N. Zhu, D. Zhang, W. Wang, X. Li, B. Yang, J. Song, X. Zhao, B. Huang, W. Shi, R. Lu, P. Niu, F. Zhan, X. Ma, D. Wang, W. Xu, G. Wu, G. F. Gao, W. Tan; China Novel Coronavirus Investigating and Research Team, A novel coronavirus from patients with pneumonia in China, 2019. *N. Engl. J. Med.* **382**, 727–733 (2020). doi:10.1056/NEJMoa2001017 Medline
2. P. Zhou, X.-L. Yang, X.-G. Wang, B. Hu, L. Zhang, W. Zhang, H.-R. Si, Y. Zhu, B. Li, C.-L. Huang, H.-D. Chen, J. Chen, Y. Luo, H. Guo, R.-D. Jiang, M.-Q. Liu, Y. Chen, X.-R. Shen, X. Wang, X.-S. Zheng, K. Zhao, Q.-J. Chen, F. Deng, L.-L. Liu, B. Yan, F.-X. Zhan, Y.-Y. Wang, G.-F. Xiao, Z.-L. Shi, A pneumonia outbreak associated with a new coronavirus of probable bat origin. *Nature* (2020). doi:10.1038/s41586-020-2012-7 Medline
3. T. M. Gallagher, M. J. Buchmeier, Coronavirus spike proteins in viral entry and pathogenesis. *Virology* **279**, 371–374 (2001). doi:10.1006/viro.2000.0757 Medline
4. G. Simmons, P. Zmora, S. Gierer, A. Heurich, S. Pöhlmann, Proteolytic activation of the SARS-coronavirus spike protein: Cutting enzymes at the cutting edge of antiviral research. *Antiviral Res.* **100**, 605–614 (2013). doi:10.1016/j.antiviral.2013.09.028 Medline
5. S. Belouzard, V. C. Chu, G. R. Whittaker, Activation of the SARS coronavirus spike protein via sequential proteolytic cleavage at two distinct sites. *Proc. Natl. Acad. Sci. U.S.A.* **106**, 5871–5876 (2009). doi:10.1073/pnas.0809524106 Medline
6. G. Simmons, J. D. Reeves, A. J. Rennekamp, S. M. Amberg, A. J. Piefer, P. Bates, Characterization of severe acute respiratory syndrome-associated coronavirus (SARS-CoV) spike glycoprotein-mediated viral entry. *Proc. Natl. Acad. Sci. U.S.A.* **101**, 4240–4245 (2004). doi:10.1073/pnas.0306446101 Medline
7. W. Song, M. Gui, X. Wang, Y. Xiang, Cryo-EM structure of the SARS coronavirus spike glycoprotein in complex with its host cell receptor ACE2. *PLOS Pathog.* **14**, e1007236 (2018). doi:10.1371/journal.ppat.1007236 Medline
8. F. Li, W. Li, M. Farzan, S. C. Harrison, Structure of SARS coronavirus spike receptor-binding domain complexed with receptor. *Science* **309**, 1864–1868 (2005). doi:10.1126/science.1116480 Medline

9. J. K. Millet, G. R. Whittaker, Host cell proteases: Critical determinants of coronavirus tropism and pathogenesis. *Virus Res.* **202**, 120–134 (2015). doi:10.1016/j.virusres.2014.11.021 Medline

10. G. Simmons, D. N. Gosalia, A. J. Rennekamp, J. D. Reeves, S. L. Diamond, P. Bates, Inhibitors of cathepsin L prevent severe acute respiratory syndrome coronavirus entry. *Proc. Natl. Acad. Sci. U.S.A.* **102**, 11876–11881 (2005). doi:10.1073/pnas.0505577102 Medline

11. M. Hoffmann, H. Kleine-Weber, N. Krüger, M. Müller, C. Drosten, S. Pöhlmann, The novel coronavirus 2019 (2019-nCoV) uses the SARS-coronavirus receptor ACE2 and the cellular protease TMPRSS2 for entry into target cells. bioRxiv 2020.01.31.929042 [Preprint]. 31 January 2020. https://doi.org/10.1101/2020.01.31.929042.

12. W. Li, M. J. Moore, N. Vasilieva, J. Sui, S. K. Wong, M. A. Berne, M. Somasundaran, J. L. Sullivan, K. Luzuriaga, T. C. Greenough, H. Choe, M. Farzan, Angiotensin-converting enzyme 2 is a functional receptor for the SARS coronavirus. *Nature* **426**, 450–454 (2003). doi:10.1038/nature02145 Medline

13. K. Kuba, Y. Imai, S. Rao, H. Gao, F. Guo, B. Guan, Y. Huan, P. Yang, Y. Zhang, W. Deng, L. Bao, B. Zhang, G. Liu, Z. Wang, M. Chappell, Y. Liu, D. Zheng, A. Leibbrandt, T. Wada, A. S. Slutsky, D. Liu, C. Qin, C. Jiang, J. M. Penninger, A crucial role of angiotensin converting enzyme 2 (ACE2) in SARS coronavirus-induced lung injury. *Nat. Med.* **11**, 875–879 (2005). doi:10.1038/nm1267 Medline

14. D. Wrapp, N. Wang, K. S. Corbett, J. A. Goldsmith, C.-L. Hsieh, O. Abiona, B. S. Graham, J. S. McLellan, Cryo-EM structure of the 2019-nCoV spike in the prefusion conformation. *Science* eabb2507 (2020). doi:10.1126/science.abb2507 Medline

15. M. Donoghue, F. Hsieh, E. Baronas, K. Godbout, M. Gosselin, N. Stagliano, M. Donovan, B. Woolf, K. Robison, R. Jeyaseelan, R. E. Breitbart, S. Acton, A novel angiotensin-converting enzyme-related carboxypeptidase (ACE2) converts angiotensin I to angiotensin 1-9. *Circ. Res.* **87**, E1–E9 (2000). doi:10.1161/01.RES.87.5.e1 Medline

16. H. Zhang, Z. Kang, H. Gong, J. W. Da Xu, Z. Li, X. Cui, J. Xiao, T. Meng, W. Zhou, J. Liu, H. Xu, The digestive system is a potential route of 2019-nCov infection: A bioinformatics analysis based on single-cell transcriptomes. bioRxiv 2020.01.30.927806 [Preprint]. 31 January 2020. https://doi.org/10.1101/2020.01.30.927806.

17. Y. Zhao, Z. Zhao, Y. Wang, Y. Zhou, Y. Ma, W. Zuo, Single-cell RNA expression profiling of ACE2, the putative receptor of Wuhan 2019-nCov. bioRxiv 2020.01.26.919985 [Preprint]. 26 January 2020. https://doi.org/10.1101/2020.01.26.919985.

18. M. A. Crackower, R. Sarao, G. Y. Oudit, C. Yagil, I. Kozieradzki, S. E. Scanga, A. J. Oliveira-dos-Santos, J. da Costa, L. Zhang, Y. Pei, J. Scholey, C. M. Ferrario, A. S. Manoukian, M. C. Chappell, P. H. Backx, Y. Yagil, J. M. Penninger, Angiotensin-converting enzyme 2 is an essential regulator of heart function. *Nature* **417**, 822–828 (2002). doi:10.1038/nature00786 Medline

19. L. S. Zisman, R. S. Keller, B. Weaver, Q. Lin, R. Speth, M. R. Bristow, C. C. Canver, Increased angiotensin-(1-7)–forming activity in failing human heart ventricles: Evidence for upregulation of the angiotensin-converting enzyme homologue ACE2. *Circulation* **108**, 1707–1712 (2003). doi:10.1161/01.CIR.0000094734.67990.99 Medline

20. M. K. Raizada, A. J. Ferreira, ACE2: A new target for cardiovascular disease therapeutics. *J. Cardiovasc. Pharmacol.* **50**, 112–119 (2007). doi:10.1097/FJC.0b013e3180986219 Medline

21. H. Zhang, J. Wada, K. Hida, Y. Tsuchiyama, K. Hiragushi, K. Shikata, H. Wang, S. Lin, Y. S. Kanwar, H. Makino, Collectrin, a collecting duct-specific transmembrane glycoprotein, is a novel homolog of ACE2 and is developmentally regulated in embryonic kidneys. *J. Biol. Chem.* **276**, 17132–17139 (2001). doi:10.1074/jbc.M006723200 Medline

22. I. Hamming, M. E. Cooper, B. L. Haagmans, N. M. Hooper, R. Korstanje, A. D. M. E. Osterhaus, W. Timens, A. J. Turner, G. Navis, H. van Goor, The emerging role of ACE2 in physiology and disease. *J. Pathol.* **212**, 1–11 (2007). doi:10.1002/path.2162 Medline

23. R. N. Kirchdoerfer, N. Wang, J. Pallesen, D. Wrapp, H. L. Turner, C. A. Cottrell, K. S. Corbett, B. S. Graham, J. S. McLellan, A. B. Ward, Stabilized

coronavirus spikes are resistant to conformational changes induced by receptor recognition or proteolysis. *Sci. Rep.* **8**, 15701 (2018). doi:10.1038/s41598-018-34171-7 Medline

24. P. Towler, B. Staker, S. G. Prasad, S. Menon, J. Tang, T. Parsons, D. Ryan, M. Fisher, D. Williams, N. A. Dales, M. A. Patane, M. W. Pantoliano, ACE2 X-ray structures reveal a large hinge-bending motion important for inhibitor binding and catalysis. *J. Biol. Chem.* **279**, 17996–18007 (2004). doi:10.1074/jbc.M311191200 Medline
25. S. Kowalczuk, A. Bröer, N. Tietze, J. M. Vanslambrouck, J. E. J. Rasko, S. Bröer, A protein complex in the brush-border membrane explains a Hartnup disorder allele. *FASEB J.* **22**, 2880–2887 (2008). doi:10.1096/fj.08-107300 Medline
26. H. F. Seow, S. Bröer, A. Bröer, C. G. Bailey, S. J. Potter, J. A. Cavanaugh, J. E. J. Rasko, Hartnup disorder is caused by mutations in the gene encoding the neutral amino acid transporter SLC6A19. *Nat. Genet.* **36**, 1003–1007 (2004). doi:10.1038/ng1406 Medline
27. R. Kleta, E. Romeo, Z. Ristic, T. Ohura, C. Stuart, M. Arcos-Burgos, M. H. Dave, C. A. Wagner, S. R. M. Camargo, S. Inoue, N. Matsuura, A. Helip-Wooley, D. Bockenhauer, R. Warth, I. Bernardini, G. Visser, T. Eggermann, P. Lee, A. Chairoungdua, P. Jutabha, E. Babu, S. Nilwarangkoon, N. Anzai, Y. Kanai, F. Verrey, W. A. Gahl, A. Koizumi, Mutations in *SLC6A19*, encoding B^0AT1, cause Hartnup disorder. *Nat. Genet.* **36**, 999–1002 (2004). doi:10.1038/ng1405 Medline
28. A. Bröer, K. Klingel, S. Kowalczuk, J. E. J. Rasko, J. Cavanaugh, S. Bröer, Molecular cloning of mouse amino acid transport system B^0, a neutral amino acid transporter related to Hartnup disorder. *J. Biol. Chem.* **279**, 24467–24476 (2004). doi:10.1074/jbc.M400904200 Medline
29. A. Penmatsa, K. H. Wang, E. Gouaux, X-ray structure of dopamine transporter elucidates antidepressant mechanism. *Nature* **503**, 85–90 (2013). doi:10.1038/nature12533 Medline
30. J. A. Coleman, E. M. Green, E. Gouaux, X-ray structures and mechanism of the human serotonin transporter. *Nature* **532**, 334–339 (2016). doi:10.1038/nature17629 Medline

31. L. Mastroberardino, B. Spindler, R. Pfeiffer, P. J. Skelly, J. Loffing, C. B. Shoemaker, F. Verrey, Amino-acid transport by heterodimers of 4F2hc/CD98 and members of a permease family. *Nature* **395**, 288–291 (1998). doi:10.1038/26246 Medline

32. R. Yan, X. Zhao, J. Lei, Q. Zhou, Structure of the human LAT1-4F2hc heteromeric amino acid transporter complex. *Nature* **568**, 127–130 (2019). doi:10.1038/s41586-019-1011-z Medline

33. Q. Lin, R. S. Keller, B. Weaver, L. S. Zisman, Interaction of ACE2 and integrin beta1 in failing human heart. *Biochim. Biophys. Acta* **1689**, 175–178 (2004). doi:10.1016/j.bbadis.2004.05.005 Medline

34. A. Shulla, T. Heald-Sargent, G. Subramanya, J. Zhao, S. Perlman, T. Gallagher, A transmembrane serine protease is linked to the severe acute respiratory syndrome coronavirus receptor and activates virus entry. *J. Virol.* **85**, 873–882 (2011). doi:10.1128/JVI.02062-10 Medline

35. A. Heurich, H. Hofmann-Winkler, S. Gierer, T. Liepold, O. Jahn, S. Pöhlmann, TMPRSS2 and ADAM17 cleave ACE2 differentially and only proteolysis by TMPRSS2 augments entry driven by the severe acute respiratory syndrome coronavirus spike protein. *J. Virol.* **88**, 1293–1307 (2014). doi:10.1128/JVI.02202-13 Medline

36. C. Drosten, S. Günther, W. Preiser, S. van der Werf, H.-R. Brodt, S. Becker, H. Rabenau, M. Panning, L. Kolesnikova, R. A. M. Fouchier, A. Berger, A.-M. Burguière, J. Cinatl, M. Eickmann, N. Escriou, K. Grywna, S. Kramme, J.-C. Manuguerra, S. Müller, V. Rickerts, M. Stürmer, S. Vieth, H.-D. Klenk, A. D. M. E. Osterhaus, H. Schmitz, H. W. Doerr, Identification of a novel coronavirus in patients with severe acute respiratory syndrome. *N. Engl. J. Med.* **348**, 1967–1976 (2003). doi:10.1056/NEJMoa030747 Medline

37. C. Yeo, S. Kaushal, D. Yeo, Enteric involvement of coronaviruses: Is faecal-oral transmission of SARS-CoV-2 possible? *Lancet Gastroenterol. Hepatol.* S2468-1253(20)30048-0 (2020). doi:10.1016/S2468-1253(20)30048-0 Medline

38. J. Jando, S. M. R. Camargo, B. Herzog, F. Verrey, Expression and regulation of the neutral amino acid transporter B^0AT1 in rat small intestine. *PLOS ONE* **12**, e0184845 (2017). doi:10.1371/journal.pone.0184845 Medline

39. J. Lei, J. Frank, Automated acquisition of cryo-electron micrographs for single particle reconstruction on an FEI Tecnai electron microscope. *J. Struct. Biol.* **150**, 69–80 (2005). doi:10.1016/j.jsb.2005.01.002 Medline

40. S. Q. Zheng, E. Palovcak, J.-P. Armache, K. A. Verba, Y. Cheng, D. A. Agard, MotionCor2: Anisotropic correction of beam-induced motion for improved cryo-electron microscopy. *Nat. Methods* **14**, 331–332 (2017). doi:10.1038/nmeth.4193 Medline

41. T. Grant, N. Grigorieff, Measuring the optimal exposure for single particle cryo-EM using a 2.6 Å reconstruction of rotavirus VP6. *eLife* **4**, e06980 (2015). doi:10.7554/eLife.06980 Medline

42. K. Zhang, Gctf: Real-time CTF determination and correction. *J. Struct. Biol.* **193**, 1–12 (2016). doi:10.1016/j.jsb.2015.11.003 Medline

43. J. Zivanov, T. Nakane, B. O. Forsberg, D. Kimanius, W. J. H. Hagen, E. Lindahl, S. H. W. Scheres, New tools for automated high-resolution cryo-EM structure determination in RELION-3. *eLife* **7**, e42166 (2018). doi:10.7554/eLife.42166 Medline

44. D. Kimanius, B. O. Forsberg, S. H. Scheres, E. Lindahl, Accelerated cryo-EM structure determination with parallelisation using GPUs in RELION-2. *eLife* **5**, e18722 (2016). doi:10.7554/eLife.18722 Medline

45. S. H. Scheres, RELION: Implementation of a Bayesian approach to cryo-EM structure determination. *J. Struct. Biol.* **180**, 519–530 (2012). doi:10.1016/j.jsb.2012.09.006 Medline

46. S. H. Scheres, A Bayesian view on cryo-EM structure determination. *J. Mol. Biol.* **415**, 406–418 (2012). doi:10.1016/j.jmb.2011.11.010 Medline

47. A. Punjani, J. L. Rubinstein, D. J. Fleet, M. A. Brubaker, cryoSPARC: Algorithms for rapid unsupervised cryo-EM structure determination. *Nat. Methods* **14**, 290–296 (2017). doi:10.1038/nmeth.4169 Medline

48. P. B. Rosenthal, R. Henderson, Optimal determination of particle orientation, absolute hand, and contrast loss in single-particle electron cryomicroscopy. *J. Mol. Biol.* **333**, 721–745 (2003). doi:10.1016/j.jmb.2003.07.013 Medline

49. S. Chen, G. McMullan, A. R. Faruqi, G. N. Murshudov, J. M. Short, S. H. W. Scheres, R. Henderson, High-resolution noise substitution to measure overfitting and validate resolution in 3D structure determination by single

particle electron cryomicroscopy. *Ultramicroscopy* **135**, 24–35 (2013). doi:10.1016/j.ultramic.2013.06.004 Medline

50. L. G. Trabuco, E. Villa, K. Mitra, J. Frank, K. Schulten, Flexible fitting of atomic structures into electron microscopy maps using molecular dynamics. *Structure* **16**, 673–683 (2008). doi:10.1016/j.str.2008.03.005 Medline
51. P. D. Adams, P. V. Afonine, G. Bunkóczi, V. B. Chen, I. W. Davis, N. Echols, J. J. Headd, L.-W. Hung, G. J. Kapral, R. W. Grosse-Kunstleve, A. J. McCoy, N. W. Moriarty, R. Oeffner, R. J. Read, D. C. Richardson, J. S. Richardson, T. C. Terwilliger, P. H. Zwart, PHENIX: A comprehensive Python-based system for macromolecular structure solution. *Acta Crystallogr. D Biol. Crystallogr.* **66**, 213–221 (2010). doi:10.1107/S0907444909052925 Medline
52. P. Emsley, B. Lohkamp, W. G. Scott, K. Cowtan, Features and development of Coot. *Acta Crystallogr. D Biol. Crystallogr.* **66**, 486–501 (2010). doi:10.1107/S0907444910007493 Medline